# The analytical and numerical stress analysis of various domes for composite pressure vessels

Z. Padovec[a,*], D. Vondráček[a], T. Mareš[a]

[a]*Department of Mechanics Biomechanics and Mechatronics, Faculty of Mechanical Engineering, Czech Technical University in Prague, Technická 4, 160 00, Prague, Czech Republic*

## Abstract

The paper describes analytical and numerical solutions for five selected domes (a spherical shell, a geodesic-isotensoid shell, a shell with zero transversal strain, a shell with zero transversal stress, and a shell with identical strain) for composite pressure vessels manufactured by means of filament (helical) winding. The stresses and strains in the domes were evaluated analytically from known equations with the use of MATLAB script for numerical evaluation and via finite element analysis (FEA) with Abaqus software and results were compared with each other. Two failure criteria, interactive and non-interactive, were chosen for the evaluation of critical areas of the shells. Moreover, the best dome shape for a given material and polar hole/equator ratio was selected for various types of failure, i.e., a loss of tightness/leakage or the failure of the fibers.
© 2022 University of West Bohemia.

*Keywords:* pressure vessel, dome, FEA, helical winding

## 1. Introduction

Various types of heads or ends can be provided for pressure vessels. With respect to metal pressure vessels, typical dome shapes comprise of hemispherical, ellipsoidal and torispherical domes [14, 20], ovaloid domes [17], plain formed heads [3] and flat ends [13]. The use of pressure vessels is essential for storage of gases/fluids at various pressures, from consumable products to advanced aerospace systems; hence, the development of composite pressure vessels (primarily aimed at achieving weight savings and high-pressure ratings) manufactured by means of filament winding technology should be done [2]. In addition, filament winding technology allows for the development of the cylindrical part of the vessel and the domes in the form of a single manufacturing operation [16]. The trajectory of the fiber path and the corresponding fiber angles cannot be chosen arbitrarily because of the requirement for stability – the geodesic condition for winding (geodesic lines connect two points along the shortest distance over the surface and no friction force is required to keep the fiber from slipping, for example, see [21]). The geodesic condition and the utilization of various mechanical properties in different directions can be applied for developing special dome shapes for filament-wound composite pressure vessels [6].

Two main theories are applied for the analytical computation of filament wound composite pressure vessels: the netting theory [23], which reduces the transfer of load upon the loading of the fibers only (the matrix does not participate in the transfer of the load), and the theory of the orthotropic continuum, which includes the influence of the matrix on the transfer of load and which allows computation with the material stiffness in tension, compression, bending, etc. [4].

Since finite element analysis (FEA) provides a powerful tool for the investigation of the complex mechanical behavior of pressure vessels [18], it was chosen for the comparison with the analytical solution.

## 2. Analytical solution

The analytical solution is based on the classical lamination theory (CLT), for example, see [19]. The assumptions for the solution comprise of:
- a linear elastic material model of the composite,
- a wall thickness $h$ that is significantly lower than the smallest radius of the shell,
- an internal pressure that leads to membrane loading in the walls of the shell,
- a composite wall that is a balanced laminate consisting of only two layers with fiber orientations of $\pm \omega$ of the same thickness and volumetric fiber contents.

For thick shells, whose thickness is comparable to the radii of curvature, more complex analytical solutions or the finite element (FE) method must be employed [12]. A thick-walled cylinder is considered where the ratio between the outer and inner radius is greater than $(1.1 \div 1.2)$, for example.

### 2.1. Stress in the composite layer

In each layer of the coordinate system $(L, T)$, the Hooke's law can be written with the use of the stiffness matrix as

$$
\begin{bmatrix} \sigma_L \\ \sigma_T \\ \tau_{LT} \end{bmatrix} = \begin{bmatrix} \frac{E_L}{1-\nu_{LT}\nu_{TL}} & -\frac{\nu_{TL}E_L}{1-\nu_{LT}\nu_{TL}} & 0 \\ -\frac{\nu_{LT}E_T}{1-\nu_{LT}\nu_{TL}} & \frac{E_T}{1-\nu_{LT}\nu_{TL}} & 0 \\ 0 & 0 & G_{LT} \end{bmatrix} \begin{bmatrix} \varepsilon_L \\ \varepsilon_{LT} \\ \gamma_{LT} \end{bmatrix}
\tag{1}
$$

or with the use of the compliance matrix as

$$
\begin{bmatrix} \varepsilon_L \\ \varepsilon_{LT} \\ \gamma_{LT} \end{bmatrix} = \begin{bmatrix} \frac{1}{E_L} & -\frac{\nu_{TL}}{E_L} & 0 \\ -\frac{\nu_{LT}}{E_T} & \frac{1}{E_T} & 0 \\ 0 & 0 & \frac{1}{G_{LT}} \end{bmatrix} \begin{bmatrix} \sigma_L \\ \sigma_T \\ \tau_{LT} \end{bmatrix},
\tag{2}
$$

where $E_L$ is the longitudinal modulus, $E_T$ is the transversal modulus, $G_{LT}$ is the shear modulus, $\nu_{LT}$ is the major Poisson ratio and $\nu_{TL}$ is the minor Poisson ratio. The knowledge of the stress and strain components in different coordinate systems, for example, $(\psi, \varphi)$ in Fig. 1, allows for the determination of the same quantities in the coordinate system $(L, T)$

$$
\begin{bmatrix} \sigma_L \\ \sigma_T \\ \tau_{LT} \end{bmatrix} = \boldsymbol{T} \begin{bmatrix} \sigma_\psi \\ \sigma_\varphi \\ \tau_{\psi\varphi} \end{bmatrix}
\tag{3}
$$

and

$$
\begin{bmatrix} \varepsilon_L \\ \varepsilon_{LT} \\ \gamma_{LT} \end{bmatrix} = \boldsymbol{T} \begin{bmatrix} \varepsilon_\psi \\ \varepsilon_\varphi \\ \frac{1}{2}\gamma_{\psi\varphi} \end{bmatrix},
\tag{4}
$$
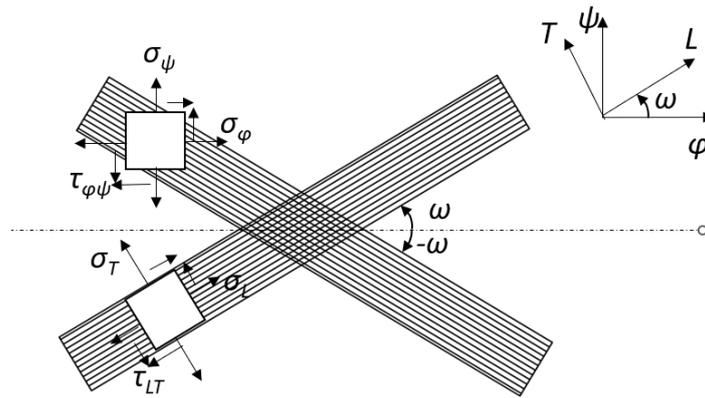
Fig. 1. The coordinate systems of the layers and their transformation

where $\boldsymbol{T}$ is the transformation matrix

$$\boldsymbol{T} = \boldsymbol{T}(\alpha) = \begin{bmatrix} m^2 & n^2 & 2mn \\ n^2 & m^2 & 2mn \\ -mn & mn & m^2 - n^2 \end{bmatrix}, \tag{5}$$

where $\alpha = \pm\omega$, $m = \cos\alpha$, $n = \sin\alpha$.

In the case of a layer, for which the loading direction differs from the orientation of the fibers, the relationship between the stress/strain is

$$\begin{bmatrix} \sigma_\psi \\ \sigma_\varphi \\ \tau_{\psi\varphi} \end{bmatrix} = \begin{bmatrix} Q_{11} & Q_{12} & Q_{16} \\ Q_{21} & Q_{22} & Q_{26} \\ Q_{61} & Q_{62} & Q_{66} \end{bmatrix} \begin{bmatrix} \varepsilon_\psi \\ \varepsilon_\varphi \\ \frac{1}{2}\gamma_{\psi\varphi} \end{bmatrix}, \tag{6}$$

where $Q_{ij}$ are the elements of a well-known reduced stiffness matrix (for example, see [13]), which can be expressed using the elastic constants of the layer in the $(L, T)$ coordinate system: $E_L$, $E_T$, $G_{LT}$, $\nu_{LT}$ and angle $\omega$. The membrane stiffness matrix $\boldsymbol{A}$ of the 2-layer laminate can be computed as

$$A_{ij} = \Big[ Q_{ij}(\omega) + Q_{ij}(-\omega) \Big] \frac{h}{2}. \tag{7}$$

The strength prediction of the computations can be expressed via the application of well-known strength theories, for example, see [5]. One non-interactive (the maximum stress failure theory [7]) and one interactive theory (the Tsai-Wu failure theory [22]) were chosen for prediction purposes. The maximum stress theory states that failure occurs when at least one of the stresses in the material coordinates exceeds the corresponding experimental strength value. This can be expressed as

$$-F_{Lc} < \sigma_L < F_{Lt}, \quad -F_{Tc} < \sigma_T < F_{Tt}, \quad -F_{LT} < \sigma_{LT} < F_{LT}. \tag{8}$$

The Tsai-Wu criterion can be stated as

$$\left( \frac{1}{F_{Lt}} - \frac{1}{F_{Lc}} \right) \sigma_L + \left( \frac{1}{F_{Tt}} - \frac{1}{F_{Tc}} \right) \sigma_T + \frac{\sigma_L^2}{F_{Lt}F_{Lc}} + \frac{\sigma_T^2}{F_{Tt}F_{Tc}} + \frac{\tau_{LT}^2}{F_{LT}^2} + 2f_{12}^* \frac{\sigma_L \sigma_T}{F_{Lt}F_{Lc}} = 1, \tag{9}$$

where

$$f_{12}^* = -\frac{1}{2} \sqrt{ \frac{1}{F_{Lt}F_{Lc}} \frac{1}{F_{Tt}F_{tc}} }. \tag{10}$$

Here, $F$ is the strength, the first subscript is the direction in the material coordinates $(L, T)$ and the second index denotes the tension/compression. In composite pressure vessels manufactured by means of helical winding, failure may occur in the form of media leakage (the fibers are without failure) or by total burst of the shell wall and failure of the fibers. The first failure is caused by the loss of adhesion between fibers and matrix or by matrix failure ($\tau_{LT}$ and $\sigma_T$ are responsible for the leakage failure) and it occurs in shells without liner or with liner which has just protective function against aggressive medium. The second type of failure occurs at significantly higher pressures when the shell wall already lost its tightness but according to the hermetic liner there is no leakage ($\sigma_L$ is responsible for the failure of the fibers) [2].

### 2.2. Stresses in the shell

Let us consider a closed pressure vessel for all the analyzed cases mentioned below. The membrane stresses (or the in-plane resultant forces) in the meridian and circumferential directions (Fig. 2) are [8]

$$\sigma_\psi = \frac{N_\psi}{h} = \frac{pR_\varphi}{2h}, \qquad \sigma_\varphi = \frac{N_\varphi}{h} = \frac{pR_\varphi}{2h} \left( 2 - \frac{R_\varphi}{R_\psi} \right), \tag{11}$$

where $p$ is the internal pressure and $R_\varphi$ and $R_\psi$ are the principal radii of curvature in the circumferential and meridian directions, respectively.

In a balanced laminate, the total $\tau_{\psi\varphi} = 0$; however, each layer exhibits a different shear stress ($+\tau_{\psi\varphi}$ and $-\tau_{\psi\varphi}$). The normal stresses $\sigma_\psi$ and $\sigma_\varphi$ are the same for the whole of the balanced laminate and for each layer. The normal stresses in each layer can be written according to (11), the shear stress in the $+\omega$ layer as

$$\tau_{\psi\varphi} = Q_{16}\varepsilon_\psi + Q_{26}\varepsilon_\varphi + Q_{66}0, \tag{12}$$

where $\varepsilon_\psi$ and $\varepsilon_\varphi$ are the strains in the meridian and circumferential directions

$$\varepsilon_\psi = \frac{1}{E_\psi} \left( \sigma_\psi - \nu_{\psi\varphi}\sigma_\varphi \right), \qquad \varepsilon_\varphi = \frac{1}{E_\varphi} \left( \sigma_\varphi - \nu_{\varphi\psi}\sigma_\psi \right), \tag{13}$$
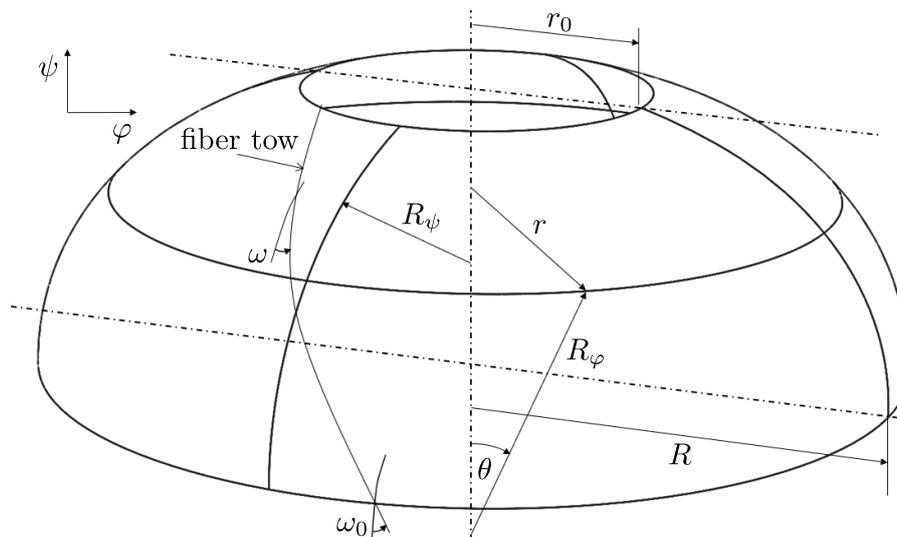


Fig. 2. Shell of revolution of double curvature geometry manufactured by means of helical winding

where $E_\psi$, $E_\varphi$, $\nu_{\psi\varphi}$ and $\nu_{\varphi\psi}$ are the elastic constants in the coordinate system $(\psi, \varphi)$ that can be evaluated from the reduced stiffness matrix

$$E_\psi = Q_{11} \left( 1 - \frac{Q_{12}^2}{Q_{11}Q_{22}} \right), \quad E_\varphi = Q_{22} \left( 1 - \frac{Q_{12}^2}{Q_{11}Q_{22}} \right),$$
$$\nu_{\psi\varphi} = \frac{Q_{12}}{Q_{22}}, \quad \nu_{\varphi\psi} = \frac{Q_{12}}{Q_{11}}, \quad G_{\psi\varphi} = Q_{66}. \tag{14}$$

The boundary conditions for the shell equator are: $R_\psi = \varrho_0$, $R_\varphi = r = R$, $h = h_0$, $\omega = \omega_0$ and $\theta = \pi/2$.

The principal radii of the shell of the revolution of double curvature can be written [11] as

$$R_\psi = -\frac{\left[ 1 + (r')^2 \right]^{\frac{3}{2}}}{r''}, \qquad R_\varphi = r \left[ 1 + (r')^2 \right]^{1/2}, \tag{15}$$

where $r'$ and $r''$ are the first and second derivatives of $r$ with respect to the meridian coordinate $\psi$. The combination of (11) and (15) provides the differential equation of the shell

$$rr'' = \left[ 1 + (r')^2 \right] \left( \frac{N_\varphi}{N_\psi} - 2 \right). \tag{16}$$

For a given ratio of the in-plane resultant forces from (11) $N_\varphi/N_\psi$ (or again with the use of (11), this ratio can be expressed via $R_\varphi/R_\psi$), it is possible to obtain the meridian profile of the shell and from (15), both principal radii via the use of numerical integration [11] or of the algorithmization of graphical method by using the curvature ratio $R_\varphi/R_\psi$ for the analyzed dome shapes [8, 10].

## 2.3. Shell of revolution of double curvature

The shell geometry and elastic constants at an arbitrary point of the meridian are functions of the winding angle $\omega$, the wall thickness $h$, the angle between the axis of revolution and normal to the shell midplane $\theta$, the parallel radius $r$ and both the principal radii, Fig. 2.

The winding angle $\omega$ is given by the geodesic condition, which can be written as [9]

$$\sin \omega = \frac{r_0}{r}. \tag{17}$$

When the equator radius $R$ is added to (17), the ratio $r_0/R$ is obtained, which is the relative size of the polar hole. This ratio determines the winding angle $\omega_0$ on the equator and on the cylindrical part of the shell that lies behind the dome.

The wall thickness is caused by the winding of a tape of a constant width on a decreasing radius $r$ from the equator to the polar hole $r_0$. The wall thickness can be computed as [10]

$$h = h_0 \frac{R \cos \omega_0}{r \cos \omega}, \tag{18}$$

where $h_0$ is the wall thickness on the equator. The angle $\theta$ can be evaluated according to Fig. 2

$$\sin \theta = \frac{r}{R_\varphi}. \tag{19}$$

### 2.4. Analyzed domes

Five domes (see Fig. 6 for their meridian shape) were chosen for the analysis and comparison purposes (with constant input parameters described in Section 3): a spherical shell, a geodesic-isotensoid shell, a shell with zero transversal strain, a shell with zero transversal stress, and a shell with identical strains.

### Spherical shell

The meridian curve of spherical shells is given, i.e., it is not a function of the elastic material parameters or the relative size of the polar hole $r_0/R$. In the whole field of the shell,

$$\frac{R_\varphi}{R_\psi} = 1. \tag{20}$$

### Geodesic-isotensoid (GI)

The dome shape is based on the netting analysis (from the condition of constant fiber tension) [24]. The meridian curve is not a function of the elastic material parameters but is unambiguously determined by the relative size of the polar hole $r_0/R$. According to the netting analysis [8, 23],

$$\frac{N_\varphi}{N_\psi} = \tan^2 \omega. \tag{21}$$

With the use of (11), (21), (17) and (16), the following formula was obtained

$$\frac{R_\varphi}{R_\psi} = \frac{2 - 3\frac{r_0^2}{r^2}}{1 - \frac{r_0^2}{r^2}} = \frac{rr''}{\left[1 + (r')^2\right]}. \tag{22}$$

From (22), it is clear that the meridian curve has an inflection point at a location where $r'' = 0$

$$r = r_0 \sqrt{\frac{3}{2}}. \tag{23}$$

This point divides the meridian curve into two parts: the wide part of the shell is concave, $r_0\sqrt{3/2} < r < R$, and the small part of the shell is convex, $r_0 < r < r_0\sqrt{3/2}$. The small convex part of the profile approximates to the sphere radius or the conical part and the polar fitting should reach beyond the inflection point [24].

### Shell with zero transversal strain $\varepsilon_T = 0$

The meridian curve is a function of the elastic material parameters and the relative size of the polar hole $r_0/R$. Zero strain applies in the transversal direction to the reinforcing fibers at each point [10]. The condition $\varepsilon_T = 0$ results in

$$\frac{R_\varphi}{R_\psi} = 2 - \frac{\frac{\nu_{\varphi\psi}}{E_\varphi} - \frac{1}{E_\psi}\tan^2\omega}{\frac{1}{E_\varphi} - \frac{\nu_{\psi\varphi}}{E_\psi}\tan^2\omega}. \tag{24}$$

### Shell with zero transversal stress $\sigma_T = 0$

The meridian curve is a function of the elastic material parameters and the relative size of the polar hole $r_0/R$. Zero stress applies in the transversal direction to the reinforcing fibers at each point [15]. The condition $\sigma_T = 0$ results in

$$\frac{R_\varphi}{R_\psi} = 2 - \frac{E_\varphi}{Q_{11}} \frac{\nu_{LT} + \tan^2\omega}{\tan^2\omega\,(\nu_{\varphi\psi} - \nu_{LT}) + \nu_{\varphi\psi}\nu_{LT} - 1} - \nu_{\varphi\psi}. \tag{25}$$

*Shell with identical strains $\varepsilon_T = \varepsilon_L$, $\varepsilon_\psi = \varepsilon_\varphi$*

The meridian curve is a function of the elastic material parameters and the relative size of the polar hole $r_0/R$. The strain should be the same in all directions at each point [11]. This condition results in

$$\frac{R_\varphi}{R_\psi} = 2 - \frac{A_{12} + A_{22}}{A_{11} + A_{12}}. \tag{26}$$

The meridian curves of the shells with zero transversal strain, zero transversal stress and with identical strains have an inflection point which occurs when the right-hand sides of (24)–(26) equal zero. All meridian curves of these shells are functions of the elastic material parameters so the position of the inflection point cannot be simply evaluated as in the case of the geodesic-isotensoid shell (23). The solution is similar to that of the geodesic-isotensoid shell, i.e., the very small convex part of the profile approximates to the sphere radius or the conical part and the polar fitting should reach beyond the inflection point [11].

## 3. Finite element analysis

Analytical and numerical solutions were determined for a glass/epoxy system (volumetric fiber content of 60 %) with the elastic and strength properties shown in Tables 1 and 2, respectively. The properties were taken from LamiEx software used by Compo Tech PLUS company. The other analysis input characteristics comprised of the radius of the polar hole $r_0 = 20$ mm, the equator radius $R = 50$ mm (i.e., $r_0/R = 0.4$, which clearly determines the winding angle $\pm \omega_0 = 23.6°$ on the equator for all the analyzed dome types), the thickness on the equator $h_0 = 1$ mm and the internal pressure $p = 1$ MPa.

Table 1. Elastic properties of the lamina in the appropriate directions

| $E_L$ [MPa] | $E_T$ [MPa] | $G_{LT}$ [MPa] | $\nu_{LT}$ [−] |
|---|---|---|---|
| 46 200 | 16 513 | 5 998 | 0.31 |

Table 2. Strength properties of the lamina in the appropriate directions

| $F_{Lt}$ [MPa] | $F_{Lc}$ [MPa] | $F_{Tt}$ [MPa] | $F_{Tc}$ [MPa] | $F_{LT}$ [MPa] |
|---|---|---|---|---|
| 1 200 | 600 | 45 | 145 | 65 |

The finite element analysis (FEA) was conducted for all the above mentioned five domes in Abaqus software. The domes were modeled as shell structures applying symmetrical boundary conditions ($u_1 = u_{r2} = u_{r3} = 0$) in the $yz$-plane and the internal pressure loading, see Fig. 3; the *lamina* was chosen for the description of the behavior of each layer of the material. The colors in Fig. 3 represent the varying properties along the meridian curve – the thickness and the winding angle (which is related to the local spherical coordinate system). From Figs. 6 and 7, it is clear that in the wide area around the equator, the wall thickness $h$ and the winding angle $\omega$ are approximately constant (wall orthotropy). Rapid increase of these parameters is around polar hole so the analytical solution here loses its validity and in real construction the polar fitting reinforce these areas. S4R shell elements (for details, see [1]) were applied for all the analyzed cases.
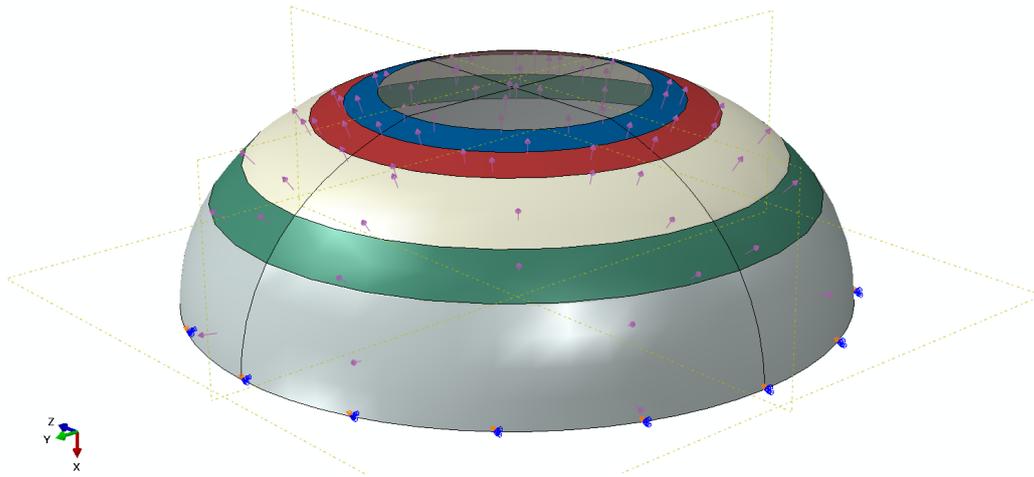
Fig. 3. The geodesic-isotensoid shell with the boundary condition and internal pressure loading

The resulting stresses must be transformed into local spherical coordinate systems in order to allow for a comparison with the analytical solutions. Fig. 4 provides an illustration of the orientation of the winding angle along the meridian curve for a shell with $\varepsilon_T = 0$.
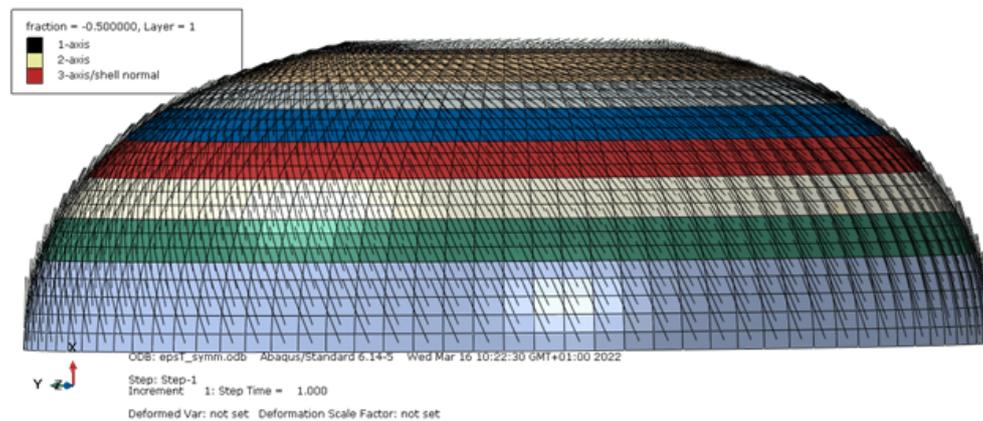


Fig. 4. The orientation of the winding angle along the meridian for the shell with $\varepsilon_T = 0$

The strength prediction was expressed via the application of two strength theories (maximum stress and Tsai-Wu) and the failure index $I_F$, which were considered in Abaqus software. Each of the stress-based failure theories defines a failure surface that surrounds the origin in a three-dimensional space $(\sigma_L, \sigma_T, \sigma_{LT})$. A failure occurs when a state of stress occurs on the surface. The failure index $K$ is used to measure the proximity to the failure surface

$$\left\{ \frac{\sigma_L}{K}, \frac{\sigma_T}{K}, \frac{\sigma_{LT}}{K} \right\} \quad \Longrightarrow \quad \text{failure index } I_F = 1.0, \tag{27}$$

i.e., $1/K$ is the scaling factor with which it is needed to multiply all of the stress components simultaneously so as to lie on the failure surface. Values of $K < 1$ indicate that the state of stress is within the failure surface (no failure), while values of $K \geq 1$ indicate failure. $K \equiv I_F$ for the maximum stress theory [1].

## 4. Results and discussion

All the graphs shown in Figs. 5–15 were obtained from a developed MATLAB code. Full lines in the graphs are results of the analytical solution from the code, isolated points are results from the FE solution taken from areas of each dome depicted in Figs. 3 and 4. The meridian curves of the analyzed domes obtained from (20), (22) and (24)–(26) are shown in Fig. 5 (in all the cases except that of the spherical shell, only the analyzed wide concave part of the curve is depicted because in the real construction of the dome, there is always some kind of polar fitting which should reach beyond the inflection point so the area between $r_0$ and the inflection point is not interesting for the presented type of analysis). The dimensionless wall thickness $h/h_0$, see (18), and the winding angle $\omega$, see (17), related to the angle $\theta$, see (19), can be noted in Figs. 6 and 7.

The normal and shear stresses, see (11) and (12), in the coordinate system $(\psi, \varphi)$ were normalized with respect to the meridian stress on the equator

$$\sigma_{eq} = \frac{pR}{2h_0} \tag{28}$$

and shown in Figs. 8–10. The strains in the meridian and circumferential directions (13) are plotted in Figs. 11 and 12.

The normalized transversal and shear stresses ($\sigma_T$, $\tau_{LT}$) in the coordinate system $(L, T)$, which are crucial in terms of the comparison of the analysed domes, can be seen in Fig. 13. The longitudinal stress $\sigma_L$ in the coordinate system $(L, T)$ was not evaluated since the strength value in this direction ($F_{Lt}$) is higher than the transversal tension strength ($F_{Tt}$) and the shear strength ($F_{LT}$).

The maximum stress and the Tsai-Wu failure index for the analyzed domes can be seen in Figs. 14 and 15. A safety factor is not used in this case, because for the case of the Tsai-Wu failure index of the shell with zero transversal stress, it has negative values close to zero and in the area with $\theta$ around $30°$, it goes from negative to positive values, so for $I_F = 0$, $K = +\infty$.
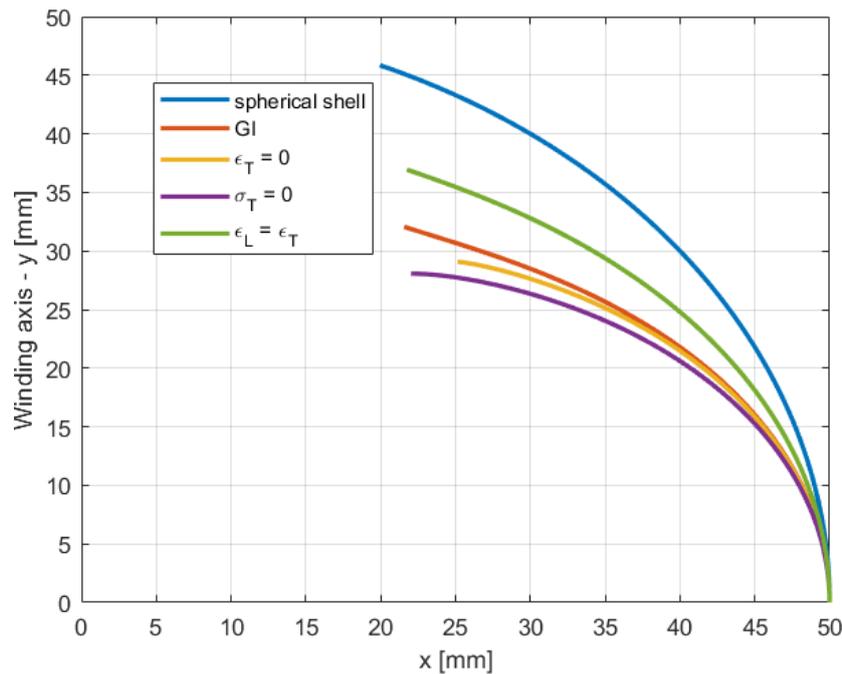


Fig. 5. The meridian curves of the analyzed domes
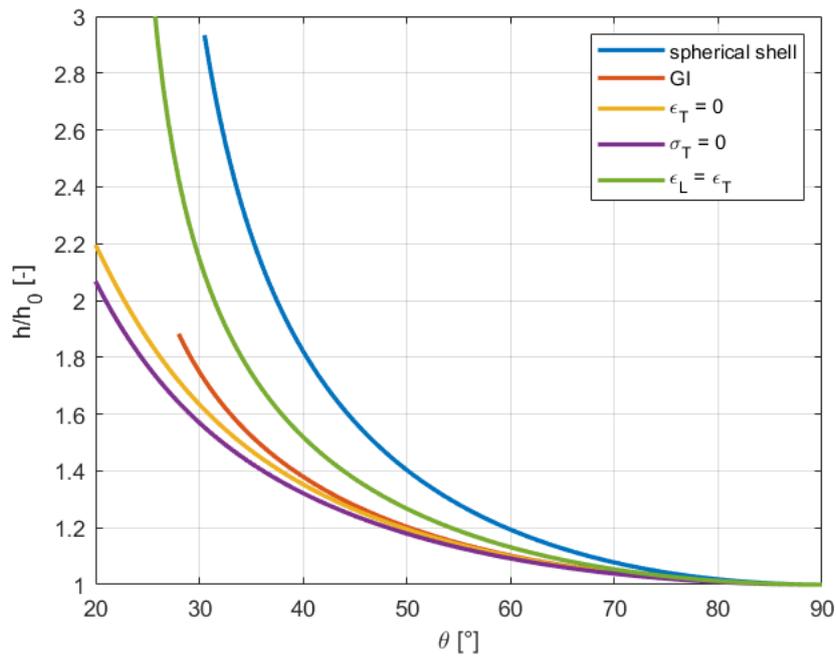
Fig. 6. The dimensionless wall thicknesses of the analyzed domes
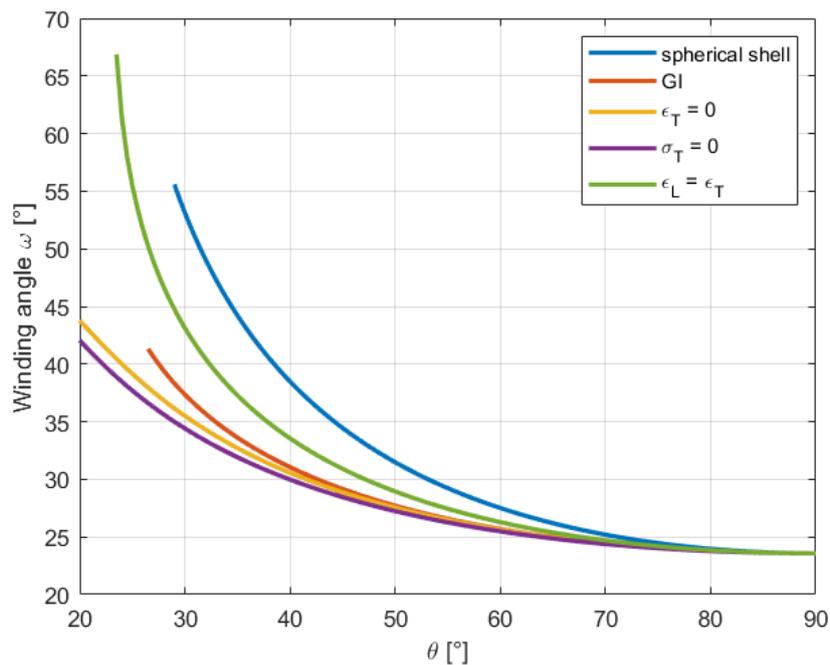


Fig. 7. The winding angle of the analyzed domes

The thick red lines in Figs. 14 and 15 stand for $I_F = 1$. Figs. 13–15 illustrate the critical areas on the analyzed domes.

The spherical shell has low $\tau_{LT}$ values; hence, $\sigma_T$ is responsible for the failure and it exhibits a maximal value on the equator – the critical area is located where the thickness of the wall is the smallest. Moreover, the figures that show $I_F$ serve to prove this fact, i.e., the maximal value of $I_F$ is on the equator. The geodesic-isotensoid (GI) shell exhibited maximal $\tau_{LT}$ and $\sigma_T$ values around the inflection point area, as confirmed by the $I_F$ figures; hence, the critical area was
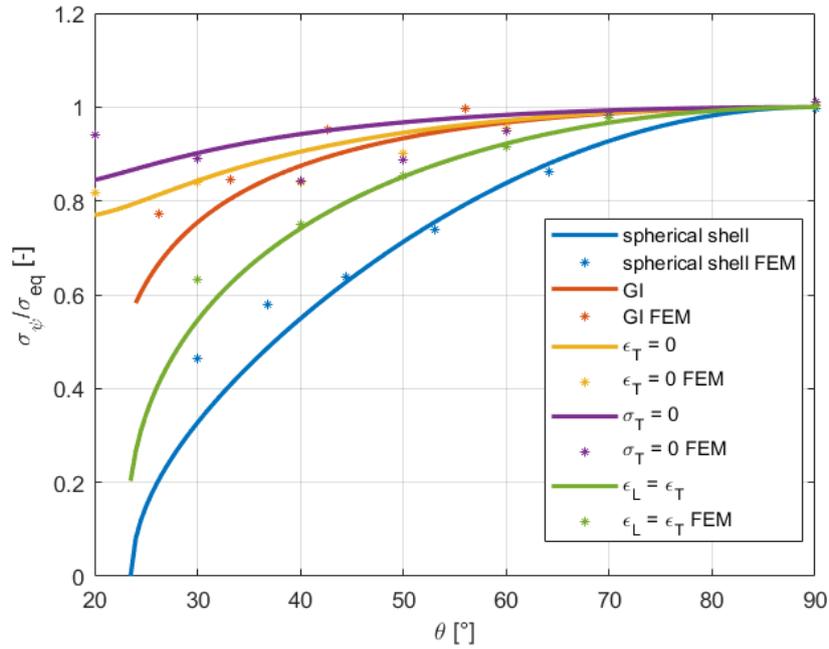
Fig. 8. The normalized $\sigma_\psi$ stress in the coordinate system $(\psi, \varphi)$ for the analyzed domes
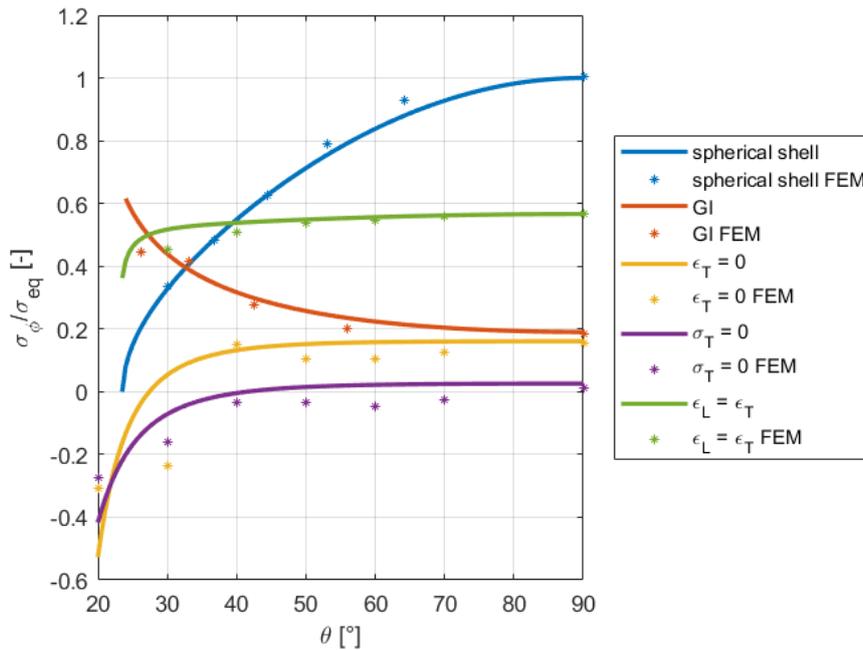


Fig. 9. The normalized $\sigma_\varphi$ stress in the coordinate system $(\psi, \varphi)$ for the analyzed domes

located around the inflection point. The shell with $\varepsilon_T = 0$ exhibited a maximal $\sigma_T$ value on the equator and the maximal $\tau_{LT}$ was near to the polar hole. The maximal $I_F$ and the critical area were around the inflection point for the value $r_0/R = 0.4$ and the given material parameters. The shell with $\sigma_T = 0$ exhibited a maximal $\tau_{LT}$, $I_F$ and a critical area around the polar hole.

The shell with $\varepsilon_T = \varepsilon_L$ has $\tau_{LT} = 0$; hence, $\sigma_T$ was responsible for the failure and exhibited a maximum value on the equator – the critical area was located where the wall thickness was the smallest. Moreover, the figures for $I_F$ confirmed this fact – the maximal $I_F$ value was on
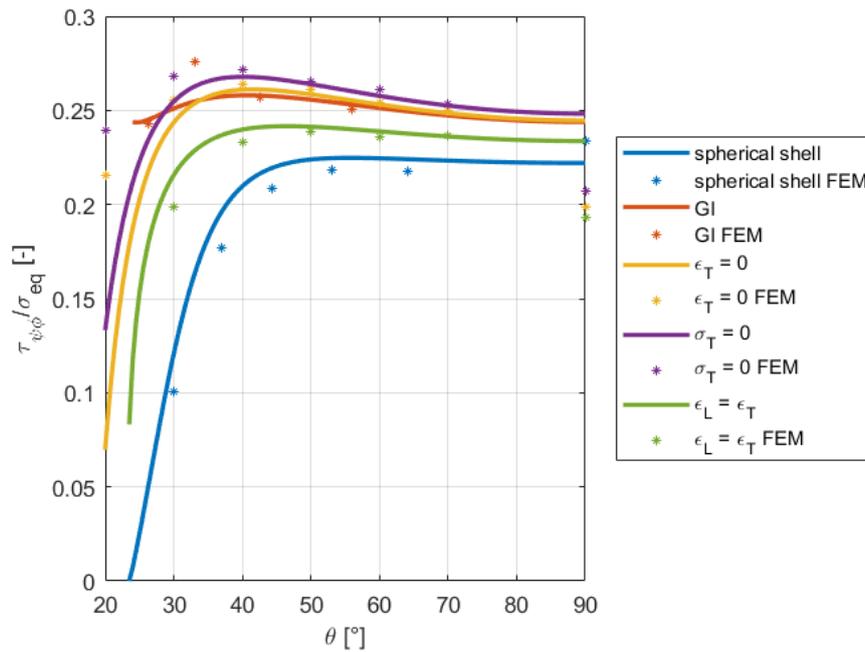
Fig. 10. The normalized shear stress $\tau_{\psi\varphi}$ in the coordinate system $(\psi, \varphi)$ for the analyzed domes
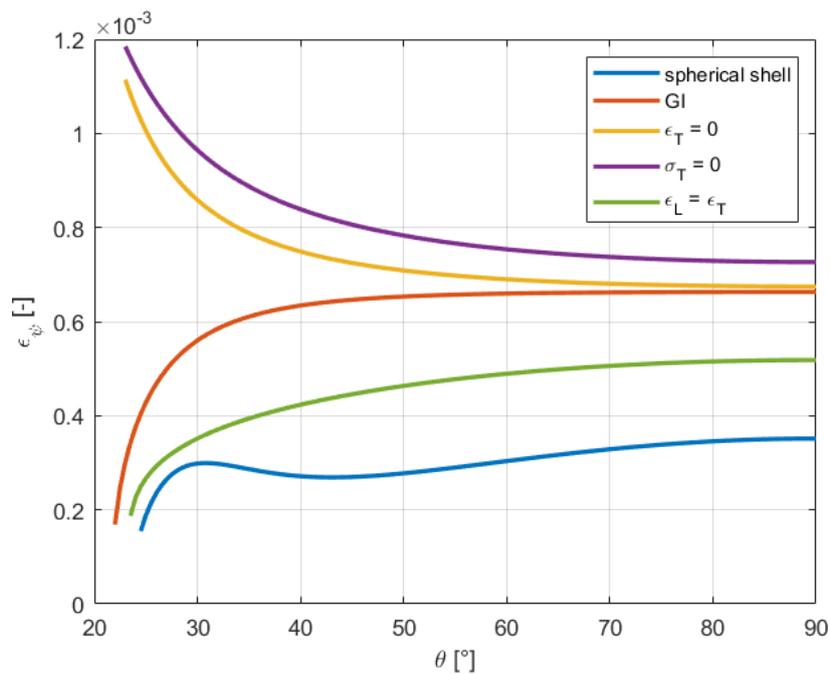


Fig. 11. The strains $\varepsilon_\psi$ in the coordinate system $(\psi, \varphi)$ for the analyzed domes

the equator.

Figs. 13–15 are useful in terms of the selection of the best shape for a given geometric $(r_0/R = 0.4)$ and material configuration from the $\tau_{LT}$ and $\sigma_T$ points of view. The $\tau_{LT}$ and $\sigma_T$ stresses were responsible for a potential leakage. From Fig. 14, it can be stated that the shell with zero transversal strain $(\varepsilon_T = 0)$ exhibited the lowest $I_F$, followed by the shell with zero transversal stress $(\sigma_T = 0)$, the geodesic-isotensoid (GI) shell, the shell with identical strains $(\varepsilon_L = \varepsilon_T)$ and finally, the spherical shell. From Fig. 15, it can be stated that the shell with zero
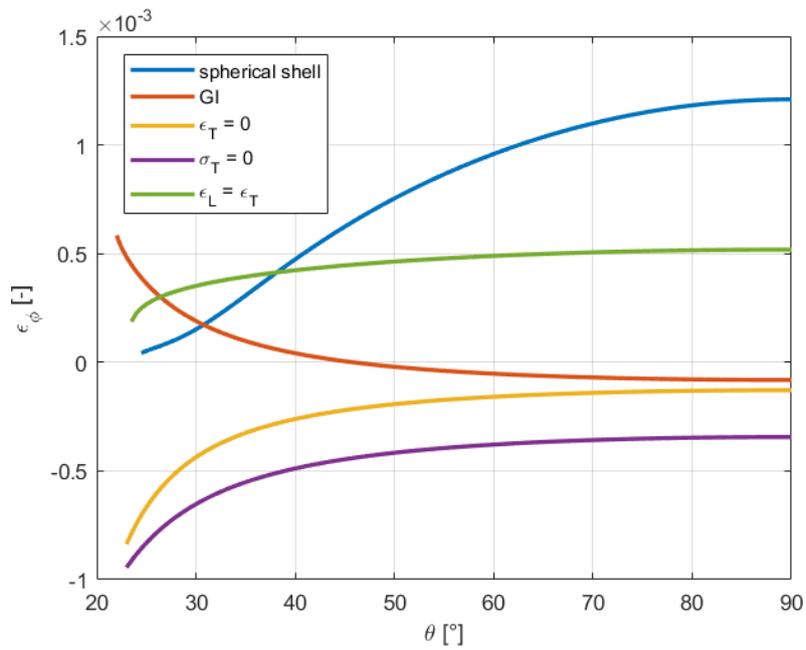
Fig. 12. The strains $\varepsilon_\varphi$ in the coordinate system $(\psi, \varphi)$ for the analyzed domes
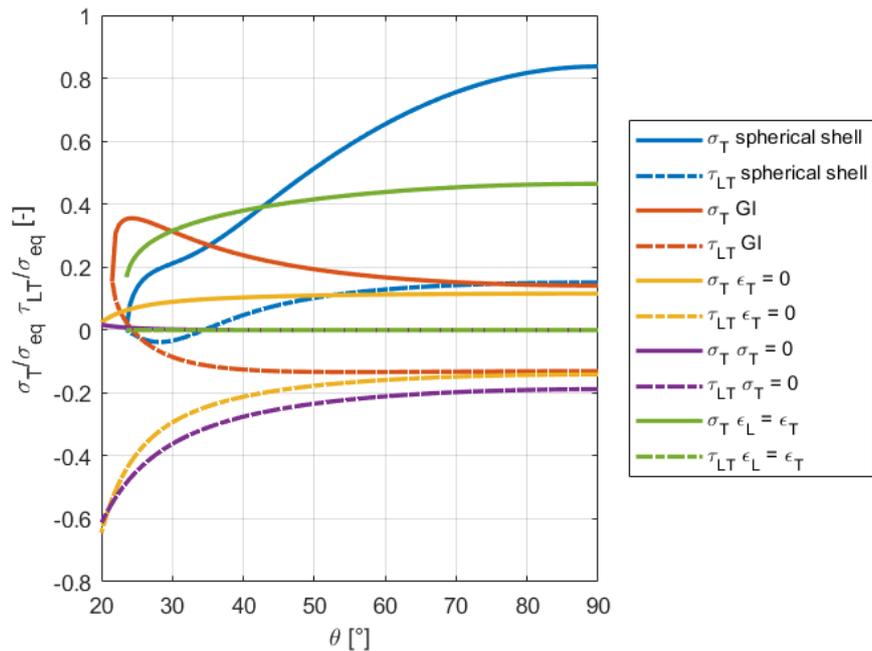


Fig. 13. The normalized transversal and shear stress in the local (material) coordinates for the analyzed domes

transversal stress ($\sigma_T = 0$) exhibited the lowest $I_F$, followed by the shell with zero transversal strain ($\varepsilon_T = 0$), the geodesic-isotensoid (GI) shell, the shell with identical strains ($\varepsilon_L = \varepsilon_T$) and finally, the spherical shell.

If the strength theory comprises the failure of fibers $\sigma_L$, the optimum choice is the geodesic-isotensoid shell since the other shapes are not isotensoidal. The differences between the other meridian shapes and the geodesic-isotensoid shape determine the advantages/disadvantages of the dome. Thus, according to Fig. 5, in terms of $r_0/R = 0.4$ and the given material parameters,
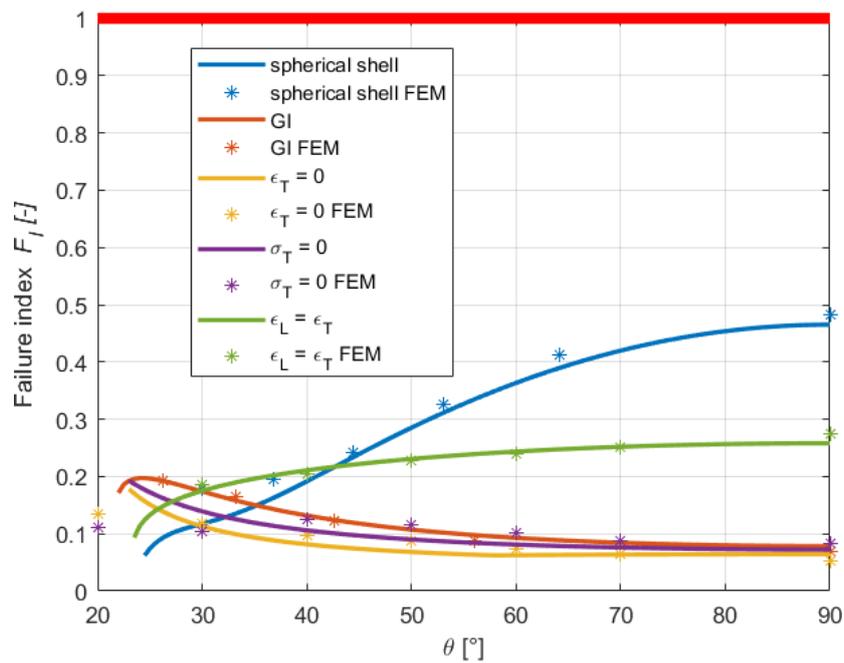
Fig. 14. The maximum stress $I_F$ for the analyzed domes
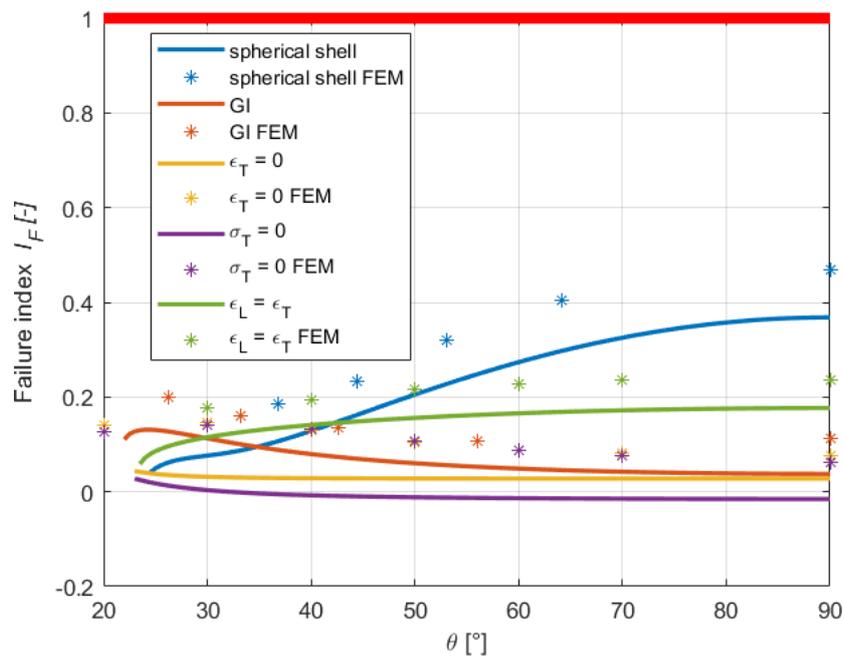


Fig. 15. The Tsai-Wu $I_F$ for the analyzed domes

the shells with zero transversal stress ($\sigma_T = 0$) and strain ($\varepsilon_T = 0$) are approximately equally advantageous, followed by the shell with identical strains ($\varepsilon_L = \varepsilon_T$) and finally, the spherical shell.

## 5. Conclusions

The analytical and numerical analysis of five shells of revolution of double curvature manufactured by means of helical winding were conducted assuming a ratio of $r_0/R = 0.4$. In the case of a spherical shell, both the analytical and numerical results indicated that failure occurs in the equator area where the wall thickness is the smallest. In the case of the other shells, specially designed for filament winding technology, failure occurs in areas that are close to the polar hole. The lowest $I_F$ (obtained by the Tsai-Wu theory) occurs in the case of the shell with zero transversal stress ($\sigma_T = 0$), followed by the shell with zero transversal strain ($\varepsilon_T = 0$), the geodesic-isotensoid (GI) shell, the shell with identical strains ($\varepsilon_L = \varepsilon_T$) and finally, the spherical shell. For the case of $I_F$ (obtained by the maximum stress theory), the order of shells with $\sigma_T = 0$ and $\varepsilon_T = 0$ is switched. It was determined that the geodesic-isotensoid shell provides the optimal solution where the failure criterion comprises the failure of the fibers. The critical areas for various types of material (fiber, matrix) may lie at different locations on the shell. Moreover, the meridian curves of the shells, which are functions of the elastic material parameters ($\varepsilon_T = 0$, $\sigma_T = 0$ and $\varepsilon_L = \varepsilon_T$), may exhibit different shapes.

An analysis was also conducted for the comparison of the analytical solution with the FEA. The analytical computations were prepared using a MATLAB code, which allows both for the rapid determination of the results and the simple changing of the input parameters (the material, the polar hole and the equator radius, the thickness and the internal pressure). The FEA provided comparable results to those of the analytical solution, particularly for an angle $\theta$ between 90° to 40° (the difference amounted to 10%). The areas defined with a lower angle $\theta$ were affected by the closure of the polar hole and the discretization of areas with constant thickness $h$. In these areas, the analytical solution also loses its validity (inflection points in some cases, principal radii growing to infinity, theoretically infinite wall thickness, etc.). Moreover, in the real construction of the dome there is always some kind of polar fitting that will reinforce these problematic areas. Changing the input parameters in the FEA is more complicated and in cases, where the shell is a function of the elastic material parameters, the computation of an analytical solution is indispensable.

Future work will focus on multicriteria optimization of several dome parameters (failure index according to a chosen strength criterion, depth of the dome, joint with the cylindrical part of the vessel, etc.).

## Acknowledgement

## References

[1] Abaqus 6.10 – Abaqus analysis user's manual, available from http://130.149.89.49:2080/v6.10/

[2] Azeem, M., Ya, H. H., Alam, M. A., Kumar, M., Stabla, P., Smolnicki, M., Gemi, L., Khan, R., Ahmed, T., Ma, Q., Sadique, M. R., Mokhtar, A. A., Mustapha, M., Application of filament winding technology in composite pressure vessels and challenges: A review, Journal of Energy Storage 49 (2022) 1–11. https://doi.org/10.1016/j.est.2021.103468

[3] Baličevič, P., Kozak, D., Mrčela, T., Strength of pressure vessels with ellipsoidal heads, Journal of Mechanical Engineering 54 (10) (2008) 685–692.

[4] Barbero, E. J., Introduction to composite materials design, CRC Press, Boca Raton, 2011. https://doi.org/10.1017/aer.2018.135

[5] Buragohain, M. K., Composite structures: Design, mechanics, analysis, manufacturing, and testing, CRC Press, Boca Raton, 2017. https://doi.org/10.1201/9781315268057

[6] Butt, A. M., Waheed-ul-Haq, S., Comparative study for the design of optimal composite pressure vessels, Key Engineering Materials 442 (2010) 462–469. https://doi.org/10.4028/www.scientific.net/KEM.442.381

[7] Chawla, K. K., Composite materials – Science and engineering, 4th edition, Springer Nature Switzerland, Cham, 2019. https://doi.org/10.1007/978-3-030-28983-6

[8] Fukunaga, H., Uemura, M., Optimum design of helically wound composite pressure vessels, Composite Structures 1 (1983) 31–49. https://doi.org/10.1016/0263-8223(83)90015-6

[9] Gay, D., Hoa, S. V., Tsai, S. W., Composite materials – Design and applications, CRC Press, Boca Raton, 2003. https://doi.org/10.1201/9781420031683

[10] Hofeditz, J. T., Structural design considerations for fibrous glass pressure vessels, Modern Plastics 41 (1964) 127–145.

[11] Hojjati, M., Ardebili, V. S., Hoa, S. V., Design of domes for polymeric pressure vessels, Composite Engineering 5 (1) (1995) 51–59. https://doi.org/10.1016/0961-9526(95)93979-6

[12] Kollár, L. P., Springer, G. S., Mechanics of composite structures, Cambridge University Press, Cambridge, 2003. https://doi.org/10.1017/CBO9780511547140

[13] Kuswah, S., Parekh, S. D., et al., Analysis of cylindrical pressure vessels with dissimilar ends and material comparison, Materials Today: Proceedings 51 (2022) 355–348. https://doi.org/10.1016/j.matpr.2021.05.466

[14] Lawate, S., Deshmukh, B. B., Analysis of heads of pressure vessel, International Journal of Innovative Research and Science Engineering and Technology 4 (2) (2015) 759–765.

[15] Love, G. G., Structural analysis of orthotropic shells, AIAA Journal 1 (8) (1963) 1843–1847. https://doi.org/10.2514/3.1933

[16] Madhavi, M., Rao, K. V. J., Rao, K. N., Design and analysis of filament wound composite pressure vessel with integrated-end domes, Defense Science Journal 59 (1) (2009) 73–81. https://doi.org/10.14429/dsj.59.1488

[17] Magnucki, K., Lewinski, J., Cichy, R., Strength and buckling problems of dished heads of pressure vessels – Contemporary look, Journal of Pressure Vessel Technology 140 (4) (2018) 1–14. https://doi.org/10.1115/1.4039844

[18] Özaslan, E., Incecik, B. B., Yetgin, A., Acar, B., Güngör, S., Sapanci, E., Güler, M. A., Experimental and numerical investigation of the cylinder-dome transition region of a pressure vessel, Composites Part C: Open Access 4 (2021) 1–5. https://doi.org/10.1016/j.jcomc.2021.100119

[19] Sharma, S., Composite materials – Mechanics, manufacturing and modeling, CRC Press, Boca Raton, 2021. https://doi.org/10.1201/9781003147756

[20] Sowiński, K., Stress distribution optimization in dished ends of cylindrical pressure vessels, Thin-Walled Structures 171 (2022) 1–17. https://doi.org/10.1016/j.tws.2021.108808

[21] Vasiliev, V. V., Composite pressure vessels: Design, analysis and manufacturing, Bull Ridge Publishing, Blacksburg, 2009. https://doi.org/10.1177/002199838401800505

[22] Wu, R. Y., Stachurski, Z., Evaluation of the normal stress interaction parameter in the tensor polynomial strength theory for anisotropic materials, Journal of Composite Materials 18 (1984) 456–463.

[23] Young, R. E., History and potential of filament winding, Proceedings of the 13th Annual Technical Conference SPI – RP, Chicago, 1958.

[24] Zickel, S., Isotensoid pressure vessels, ARS Journal 32 (1962) 950–951.